CrossMark

J. Fluid Mech. (2020), *vol*. 905, R1, doi:10.1017/jfm.2020.778



Laminar separated flows over finite-aspect-ratio swept wings

Kai Zhang[1],†, Shelby Hayostek[2], Michael Amitay[2], Anton Burtsev[3], Vassilios Theofilis[3,4] and Kunihiko Taira[1]

[1]Department of Mechanical and Aerospace Engineering, University of California, Los Angeles, CA 90095, USA

[2]Department of Mechanical, Aeronautical, and Nuclear Engineering, Rensselaer Polytechnic Institute, Troy, NY 12180, USA

[3]Department of Mechanical, Materials and Aerospace Engineering, University of Liverpool, Brownlow Hill, Liverpool L69 3GH, UK

[4]Department of Mechanical Engineering, Escola Politecnica, Universidade São Paulo, Avda. Prof. Mello Moraes 2231, CEP 5508-900 São Paulo, Brasil

(Received 19 May 2020; revised 30 July 2020; accepted 10 September 2020)

We perform direct numerical simulations of laminar separated flows over finite-aspect-ratio swept wings at a chord-based Reynolds number of $Re = 400$ to reveal a variety of wake structures generated for a range of aspect ratios (semi aspect ratio $sAR = 0.5$–4), angles of attack ($\alpha = 16^\circ$–30°) and sweep angles ($\Lambda = 0^\circ$–45°). Flows behind swept wings exhibit increased complexity in their dynamical features compared to unswept-wing wakes. For unswept wings, the wake dynamics are predominantly influenced by the tip effects. Steady wakes are mainly limited to low-aspect-ratio wings. Unsteady vortex shedding takes place near the midspan of higher-AR wings due to weakened downwash induced by the tip vortices. With increasing sweep angle, the source of three-dimensionality transitions from the tip to the midspan. The three-dimensional midspan effects are responsible for the formation of the stationary vortical structures at the inboard part of the span, which expands the steady wake region to higher aspect ratios. At higher aspect ratios, the midspan effects of swept wings diminish at the outboard region, allowing unsteady vortex shedding to develop near the tip. In the wakes of highly swept wings, streamwise finger-like structures form repetitively along the wing span, providing a stabilizing effect. The insights revealed from this study can aid the design of high-lift devices and serve as a stepping

† Present address: Department of Mechanical and Aerospace Engineering, Rutgers University.
Email address for correspondence: kai.zhang3@rutgers.edu

© The Author(s), 2020. Published by Cambridge University Press

https://doi.org/10.1017/jfm.2020.778 Published online by Cambridge University Press

stone for understanding the complex wake dynamics at higher Reynolds numbers and those generated by unsteady wing manoeuvres.

Key words: separated flows, wakes, vortex dynamics

1. Introduction

Separated flows over lifting surfaces have been studied extensively due to their critical importance in aerodynamics and hydrodynamics. Over the past few decades, substantial studies have been dedicated to the understanding of post-stall flows over finite-aspect-ratio wings (Winkelmann *et al.* 1980; Taira & Colonius 2009; Mulleners, Mancini & Jones 2017; Eldredge & Jones 2019; Zhang *et al.* 2020). For a steadily translating wing, the vortices generated from the leading and trailing edges exhibit complex nonlinear evolution under the influence of the tip vortices. The resulting wake is highly three-dimensional in nature.

The introduction of sweep to the finite-aspect-ratio wings further enriches the wake dynamics. Harper & Maki (1964) asserted that, once local stall appears on the swept wing, the spanwise boundary layer flow alters the stall characteristics of the attached sections of the span. Thus the separated flows over swept wings bear little resemblance to the two-dimensional (2-D) flows. The stalled flow over a swept wing usually features a 'ram's horn' vortex, which stems from the inboard leading edge and grows in size as it trails to the wake behind the tip. Such unique flow is also referred to as 'tip stall' (Black 1956; Zhang *et al.* 2019). Focusing on the detailed flow structures, Yen & Hsu (2007) and Yen & Huang (2009) experimentally studied the effects of sweep angle, Reynolds number (Re) and angle of attack on the wake vortices, boundary layer flow patterns and aerodynamic performance of swept wings. The wake features were found to be significantly dependent on these parameters. Visbal & Garmann (2019) conducted large-eddy simulation (LES) of flows over swept wings with a semi aspect ratio (sAR) of 4 at $Re = 2 \times 10^5$. A region of laminar flow is observed near the midspan, and it grows in extent with increasing sweep angle. The authors attributed this observation to the relief effect provided by the sweep-induced spanwise flow towards the tip. Furthermore, dynamic stall was numerically simulated for a swept wing undergoing pitching and plunging manoeuvres (Visbal & Garmann 2019; Garmann & Visbal 2020). Under these unsteady motions, the release of the arch-shaped vortices during downstroke occurs near both tip regions, whereas only a single arch vortex is seen to detach from the midspan in the unswept case.

Some swept wings are well known for harnessing the separated flows to enhance their aerodynamic performance. Delta wings can generate a pair of leading-edge vortices (LEVs) to produce high lift, enabling them to operate at much higher angles of attack than conventional wings. These stationary vortices are formed due to the balance of vorticity generation along the leading edge and the vorticity transportation through the spanwise flow (Polhamus 1966; Rockwell 1993; Gursul, Gordnier & Visbal 2005). Such a mechanism is also thought to contribute to avian flights. Videler, Stamhuis & Povel (2004) identified LEVs in the swept wings of common swifts (*Apus apus*) during gliding. Lambert *et al.* (2019) investigated the formation of LEVs on swept wings with different leading-edge geometries. Their results showed similar LEV characteristics for swept wings with either straight or curved leading edges. Ben-Gida, Gurka & Weihs (2020) proposed a pseudo-three-dimensional flow model for investigating the stationary LEV mechanism over swept-back wings. The model revealed that wing geometry has a major role in the localization of the stationary LEVs over high-aspect-ratio wings. On the

https://doi.org/10.1017/jfm.2020.778 Published online by Cambridge University Press

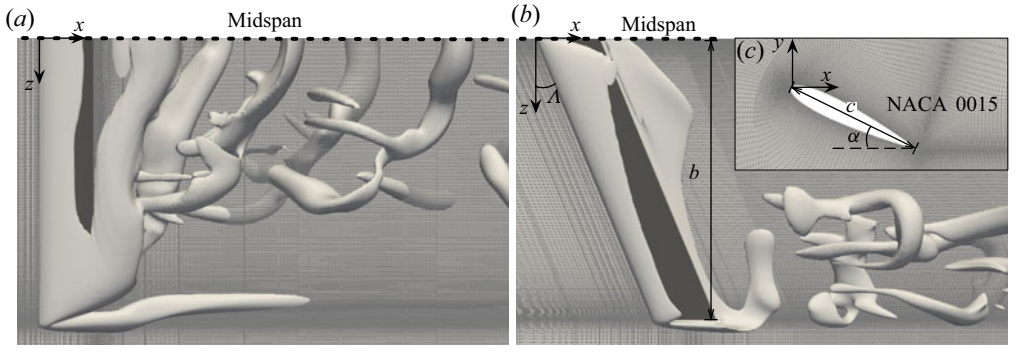


FIGURE 1. Case set-up and mesh design for (*a*) unswept wing $(sAR, \alpha, \Lambda) = (4, 26^\circ, 0^\circ)$ and (*b*) swept wing $(sAR, \alpha, \Lambda) = (4, 26^\circ, 22.5^\circ)$. The vortical structures are visualized by isosurfaces of $Qc^2/U_\infty^2 = 1$. (*c*) Near-wing mesh in cross-sectional (x–y) plane.

other hand, experimental studies by Lentink & Dickinson (2009) and Beem, Rival & Triantafyllou (2012) showed that the spanwise flow alone cannot sustain stationary LEVs for a translating swept wing. Moreover, the effectiveness of the LEVs in augmenting lift of swift wings is still arguable for low-speed flight (Lentink *et al.* 2007). These mixed findings regarding the role of separated flows over swept wings warrants further investigations.

The aforementioned studies revealed that detailed features of separated flows over swept wings depend on various parameters, including the aspect ratio, angle of attack and sweep angle. The interplay between these effects generates complex wake dynamics, which are not thoroughly understood to date. In this work, we present an extensive numerical study on the separated flows over swept wings at low Reynolds number. The objective is to characterize the different wake structures observed over a large range of parameters, and to identify their formation mechanisms. The rest of the paper is organized as follows. We present the computational set-up in § 2. A variety of wakes observed from this study is reported in § 3, and their formation mechanisms explained. We conclude this study by summarizing our findings in § 4.

2. Computational set-up

We consider three-dimensional incompressible flows over swept finite-aspect-ratio wings with the NACA 0015 cross-section profile. The set-up of the wing geometry is shown in figure 1. The wings are subjected to uniform flow with velocity U_∞ in the x direction. The z axis aligns with the spanwise direction of an unswept wing, and the y axis points in the lift direction. For the swept wings, the sweep angle Λ is defined as the angle between the z axis and the leading edge of the wing. We consider a range of sweep angles from 0° to 45°, at an interval of 7.5°. Half of the swept-wing model is simulated by prescribing a symmetry boundary condition along the midspan. Denoting the half wing span as b and the chord length as c, the semi aspect ratio is defined as $sAR = b/c$, which is varied from 0.5 to 4. We focus on the separated flows that develop behind wings at high angles of attack, $\alpha = 16^\circ$, 20°, 26° and 30°. The Reynolds number, which is defined as $Re \equiv U_\infty c/\nu$ (where ν is the kinematic viscosity), is kept fixed at 400. In what follows, all spatial variables are scaled by the chord length c, velocity by free-stream velocity U_∞ and time by c/U_∞.

https://doi.org/10.1017/jfm.2020.778 Published online by Cambridge University Press

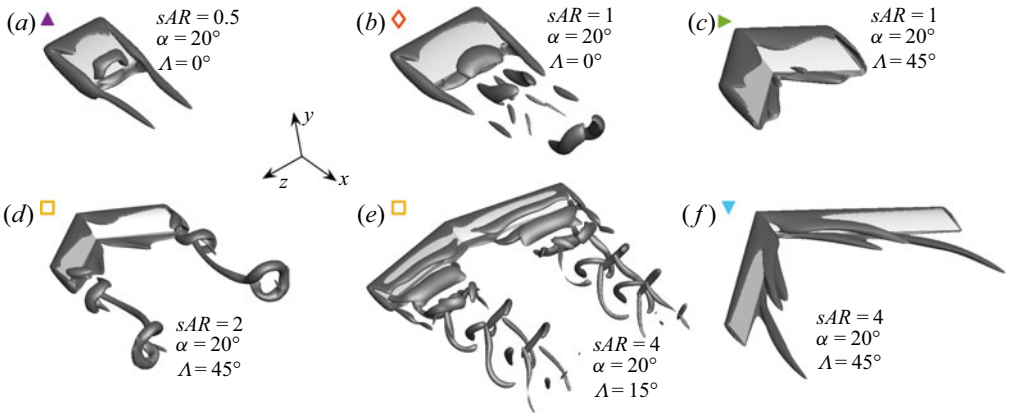


FIGURE 2. Representative wakes of swept wings visualized by isosurfaces of $Qc^2/U_\infty^2 = 1$: (*a*) steady flow with tip vortex, violet upward-pointing triangle; (*b*) unsteady shedding near midspan, orange diamond; (*c*) steady flow with midspan structures, green right-pointing triangle; (*d*,*e*) unsteady shedding near wing tip, yellow square; and (*f*) steady flow with streamwise vortices, cyan downward-pointing triangle. The figures are scaled for visual clarity.

The flows over swept wings are simulated by numerically solving the three-dimensional Navier–Stokes equations. An incompressible solver *Cliff* (in the *CharLES* software package; Cascade Technologies, Inc.) is used for the direct numerical simulations. The solver employs a collocated, node-based finite-volume method to compute the solutions to the governing equations with second-order accuracy in both space and time (Ham & Iaccarino 2004; Ham, Mattsson & Iaccarino 2006). The computational domain and the spatial discretization set-up in this study follow our previous work with extensive validation (Zhang *et al.* 2020). For the swept cases, the straight-wing mesh system is sheared in the x direction along with the wing, as shown in figure 1(*b*).

3. Results

The wakes of swept wings exhibit a rich variety of features depending on the aspect ratio, angle of attack and sweep angle. We show representative wakes in figure 2, with their distributions over the Λ–α space in figure 3 for different aspect ratios. The wakes are broadly divided into two categories: steady flows and unsteady flows. Steady flows take different forms, including those with tip vortices (violet upward-pointing triangle), those with midspan structures (green right-pointing triangle) and those with streamwise vortices (cyan downward-pointing triangle). The steady flow regime appears over a wide range of the parameter space. Unsteady flows are characterized by vortex shedding near the midspan (orange diamond) or near the tip (yellow square). The vortical structures are visualized by isosurfaces of $Qc^2/U_\infty^2 = 1$. The current classification of the wake patterns is insensitive to the exact value of the Q criterion for the examined range of 0.5–2. To determine the unsteady/steady boundaries in figure 3, we have also supplemented the analysis with the time series of the lift coefficients. In what follows, we describe key mechanisms that are responsible for the formation of the different wakes mentioned above.

3.1. *Tip effects*

Tip effects play an important role in the development of wakes behind low-aspect-ratio wings. At $sAR = 0.5$, steady flows are observed up to $\alpha = 26^\circ$, as shown in figure 3(*a*).

https://doi.org/10.1017/jfm.2020.778 Published online by Cambridge University Press

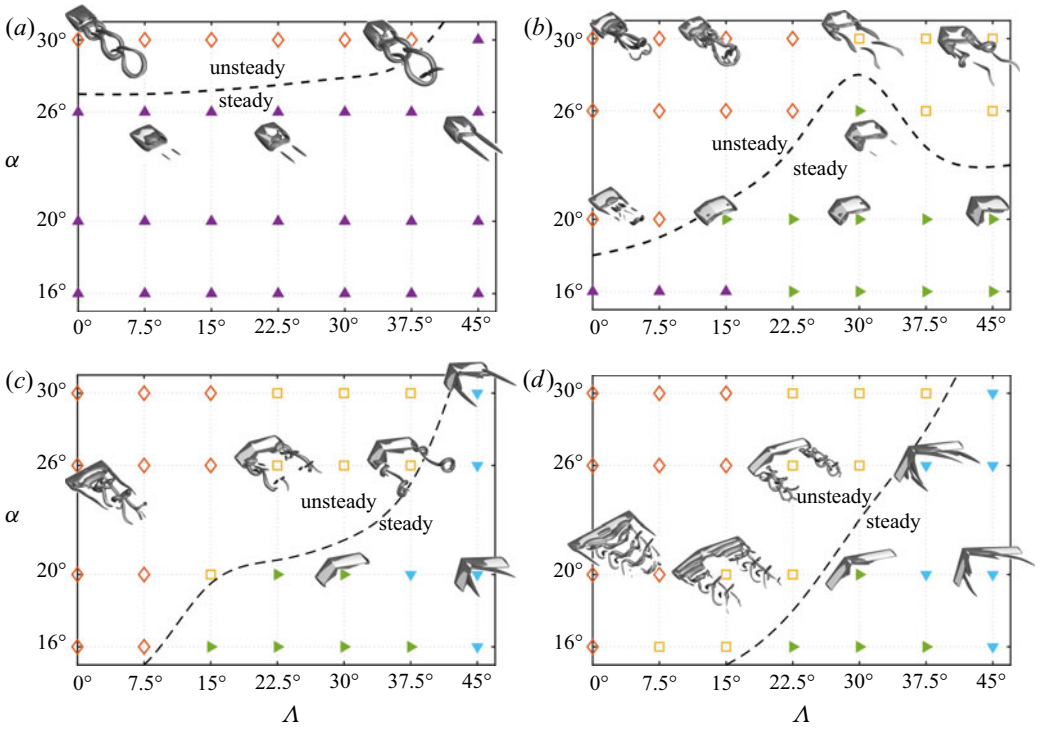


FIGURE 3. Classification of vortical structures behind finite-aspect-ratio swept wings for: (*a*) $sAR = 0.5$; (*b*) $sAR = 1$; (*c*) $sAR = 2$; and (*d*) $sAR = 4$. The dashed lines denote the approximate boundaries between steady (filled symbols) and unsteady (empty symbols) flows over the Λ–α space. Vortical structures are visualized by isosurfaces of $Qc^2/U_\infty^2 = 1$ for select cases.

These steady flows typically feature a pair of tip vortices, which induce strong downwash over the wing span, suppressing the formation of large LEVs. Such a mechanism is responsible for the stability of the wake, particularly for low-aspect-ratio unswept wings (Taira & Colonius 2009; DeVoria & Mohseni 2017; Zhang *et al.* 2020). At higher sweep angles, the vortical structures that emanate from the leading edge grow in size, covering a significant portion of the suction surface of the wing. These vortical structures are also beneficial to the stability of the wake, as will be discussed in detail in § 3.2. Unsteady flows are observed only at $\alpha \gtrsim 30°$ for $\Lambda = 0°$–$37.5°$. These unsteady wakes are characterized by the periodic shedding of hairpin vortices (Taira & Colonius 2009).

As the aspect ratio is increased, the downwash induced by the tip vortices weakens along the midspan, allowing the roll-up of the vortex sheet at the leading edge. As a result, unsteady vortex shedding develops near the midspan, as visualized in figure 2(*b*). The stability boundary (dashed line in figure 3) shifts towards lower angles of attack at $sAR = 1$ and 2 for low-swept wings. Additional details on the three-dimensional unsteady wake dynamics of wings under tip effects are reported in Taira & Colonius (2009) and Zhang *et al.* (2020).

3.2. *Midspan effects*

For wings with larger aspect ratio ($sAR \gtrsim 1$), in place of the weakened tip effects, the midspan symmetry introduces another type of three-dimensionality that dominates

https://doi.org/10.1017/jfm.2020.778 Published online by Cambridge University Press

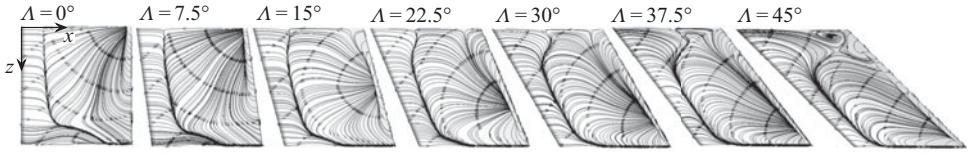


FIGURE 4. Skin-friction lines on the suction side of wings with $(\alpha, sAR) = (20^\circ, 1)$.

the wake. We present the skin-friction lines for cases of $(\alpha, sAR) = (20^\circ, 1)$ with varying Λ as shown in figure 4. With the increase in sweep angle, the leading-edge boundary layer separation point near the midspan gradually shifts towards the trailing edge. This is caused by the growth of the vortical structures emanating from the leading edge, as observed in figure 3(*b*). The increase in sweep angle for $sAR \gtrsim 1$ also leads to the attenuation of the tip vortices, as reflected by the diminishing three-dimensional skin-friction line pattern near the wing tip in figure 4. In addition, the reattachment of the separated recirculating flow, which occurs near the trailing edge, shifts away from the midspan towards the tip with increasing sweep angle. The above observations suggest a switch-over of the source of three-dimensionality from the wing tip in low-Λ cases to the midspan in high-Λ cases.

Let us take a closer look at the vortical structures near the midspan. A representative case of $(\alpha, sAR, \Lambda) = (20^\circ, 2, 45^\circ)$ is shown in figure 5. For this case, the vortex sheet rolls up along the spanwise direction, covering the entire chord over the inboard section of the wing. Owing to the symmetry condition, the identical vortical structures on the two sides of the mid-plane are oriented at an angle of $180^\circ - 2\Lambda$, which in the current case is 90°. As a result, each of the vortical structures is subjected to the downward velocity (pointing at $-y$ direction) induced by its symmetric peer on the other side of the midspan. This is clearly manifested in figure 5(*b*) by the strong negative cross-flow velocity u_y on the suction side near the $z = 0$ plane.

Owing to the three-dimensional midspan effects described above, the vortical structures near the midspan are stabilized by the downward velocity induced from themselves. For cases with smaller Λ, the angle between the symmetric vortical structure tends towards 180°, and the mutually induced velocity becomes smaller. The three-dimensionality developed from the midspan is able to stabilize the wakes of a considerable number of cases, as labelled by the green triangle in figure 3. The midspan effects are also observed for swept wings with $sAR = 0.5$, in which cases the tip vortices also stabilize the wake. In fact, the strengthening of the tip vortices with increasing Λ at $sAR = 0.5$ (see figure 3*a*, $\alpha = 26^\circ$, for example) is likely to be related to the three-dimensional midspan effects. As vortex sheets emanating from the leading edge are less likely to roll up due to the midspan effects, they counteract less on the formation of tip vortices. We note that spanwise vorticity transport, which is considered as the key mechanism for the formation of steady LEVs on delta wings (Polhamus 1966; Gursul 2005), does not play an important role in the formation of the midspan vortical structures in the current case. This is manifested by the fact that the strong outboard velocity u_z does not coincide with the vortex core, as shown in figure 5(*c*).

The downward induced velocity described above is strong near the midspan, as shown in figure 5(*b*). With the gradual weakening of the midspan effects towards the outboard sections, unsteadiness develops locally near the tip region, while the midspan region still remains steady. The resulting flows resemble the 'tip stall' phenomenon, as described in Black (1956), Zhang *et al.* (2019) and Visbal & Garmann (2019). This type of flow, as indicated by yellow squares in figure 3, prevails for swept wings with large aspect ratios

https://doi.org/10.1017/jfm.2020.778 Published online by Cambridge University Press

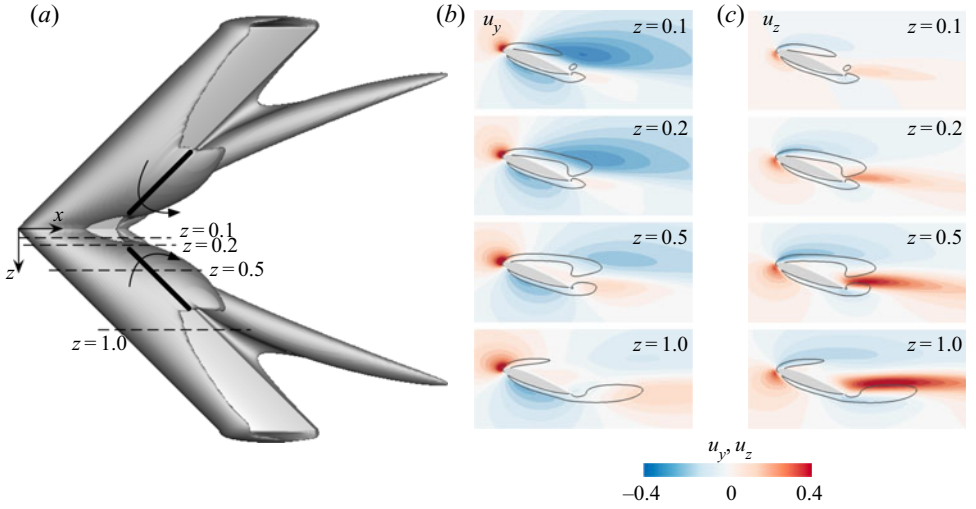


FIGURE 5. Wake for the case $(sAR, \alpha, \Lambda) = (2, 20^\circ, 45^\circ)$. (*a*) Vortical structures visualized by isosurface of $Qc^2/U_\infty^2 = 1$. The thick solid lines represent the approximate location of vortical structures near the midspan, with the curved arrows showing their directions of rotation. The dashed lines indicate the locations of visualizations shown on the right. (*b*,*c*) The u_y and u_z fields, respectively, at different z locations.

(e.g. $sAR = 4$) and high angles of attack (e.g. $\alpha = 26^\circ$–30°). For wings with large sAR, the unsteady shedding develops from the leading edge and features mostly spanwise vortices (see figure 2*e*, for example). In contrast, for wings with low aspect ratio but large angles of attack, the unsteady vortices are shed from the wing tip, and they feature hairpin structures with the legs originated from the pressure and suction sides of the wing, as shown in figure 2(*f*).

3.3. *Formation of streamwise finger-like structures*

For high sweep angles of $\Lambda \gtrsim 37.5^\circ$, the flows over high-aspect-ratio wings ($sAR \gtrsim 2$) transition from the unsteady tip shedding to steady wakes, through the formation of the streamwise finger-like structures. As shown in figure 2(*f*), the finger-like structures are oriented at an angle higher than Λ with respect to the z axis. These structures bend towards the streamwise direction away from the wing. Wakes of swept wings with even sAR as large as 10 are stabilized with the alternating formation of the streamwise structures along the wing span, as shown in figure 6(*a*).

These streamwise vortices observed in the present work are formed under the same mechanism as those in the wakes of axisymmetric slender bodies at high incidence (Sarpkaya 1966; Thomson & Morrison 1971). The impulse flow analogy has long been used to understand these vortical structures. According to this analogy, the progressive development of the wake along the wing span when viewed in cross-flow planes is similar to the temporal growth of the flow behind a 2-D wing translated impulsively from rest. Three slices at different spanwise locations in figure 6(*b*) show a temporal-like evolution of wake vortices along the wing span. In addition, the spacing between the neighbouring streamwise vortices is fixed at $g = 2.4$, which follows $g \approx U_\infty \sin(\Lambda) T_{2D}$, in which $U_\infty \sin(\Lambda)$ represents the speed of the spanwise flow, and $T_{2D} = 3.2$ is the non-dimensional period of vortex shedding in the analogous 2-D case (for an infinite

https://doi.org/10.1017/jfm.2020.778 Published online by Cambridge University Press

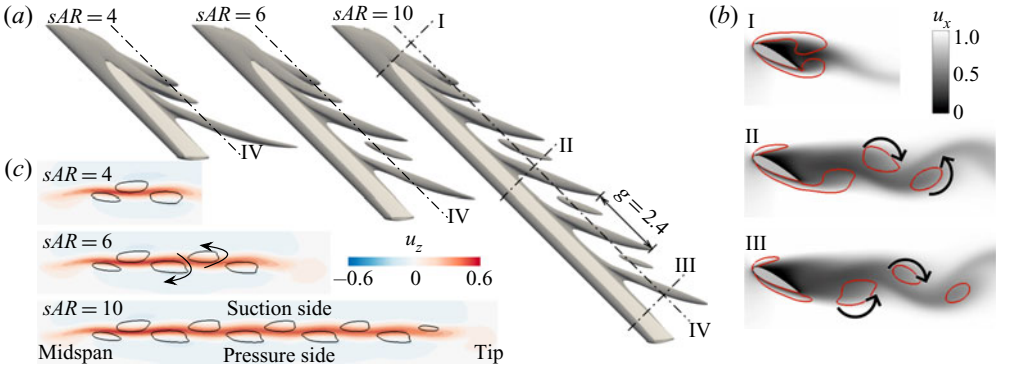


FIGURE 6. Streamwise vortices along high-aspect-ratio wings with $\Lambda = 45^\circ$. (*a*) Vortical structures visualized by isosurface of $Qc^2/U_\infty^2 = 1$ for $sAR = 4$, 6 and 10. (*b*) The u_x field at indicated slices as shown in (*a*). The red lines represent contours of $Qc^2/U_\infty^2 = 0.5$ with the curved arrows indicating the direction of rotation. (*c*) The u_z field on the slices IV for cases with three aspect ratios. Black circles show the isosurfaces of $Qc^2/U_\infty^2 = 0.5$.

swept wing). This relationship suggests a close analogy between the 2-D unsteady flow and the present three-dimensional steady flow, where the time dependence of the former is replaced by the spatial dependence of the latter.

We also plot the velocity component u_z on the planes that are parallel to the wing span in figure 6(*c*). The profiles of u_z, as well as the arrangement of the streamwise vortices, are almost identical along the spanwise direction for the wakes behind the wings with the three aspect ratios. These finger-like vortices are positioned at two sides of strong outboard velocity u_z, resembling the configuration where an inverse von Kármán vortex street is formed in a jet profile. This observation suggests the important role of the spanwise velocity in the formation of steady three-dimensional vortices. Similar streamwise structures have also been reported for rotating large-*AR* wings (Jardin 2017), in which spanwise flow is promoted by artificially adding Coriolis force.

3.4. *Aerodynamic forces*

The vortical structures described above influence the aerodynamic forces on the swept wings. We examine the effects of sweep angle on the distribution of the time-averaged sectional lift coefficients $\overline{C_l}$ for the representative cases of $(\alpha, sAR) = (20^\circ, 2)$ in figure 7(*a*). For the unswept wing, the sectional lift increases slowly from the midspan towards outboard, reaching a maximum at $z \approx 1.5$ before its drastic decrease at the tip. The slight swell-up of the sectional lift at the outboard location is attributed to downwash from the tip vortices (DeVoria & Mohseni 2017; Zhang *et al.* 2020). For swept wings, the sectional lift coefficients are significantly higher at the inboard locations. Such high lift is achieved due to the midspan effects, which trap additional vorticity in the vicinity of the suction surface (as described in § 3.2), thus increasing the local circulation. We note that the lift distribution of swept wings in high-*Re* flows exhibits the opposite pattern, where sectional lift is low near midspan and high at outboard sections (Schlichting & Truckenbrodt 1960; Nickel & Wohlfahrt 1994). Moreover, for the same angle of attack, one sees lift loss everywhere along the span of the swept wing compared with the unswept wing (Visbal & Garmann 2019). These differences highlight the midspan effects in augmenting lift of swept wings in low-Reynolds-number separated flows.

https://doi.org/10.1017/jfm.2020.778 Published online by Cambridge University Press

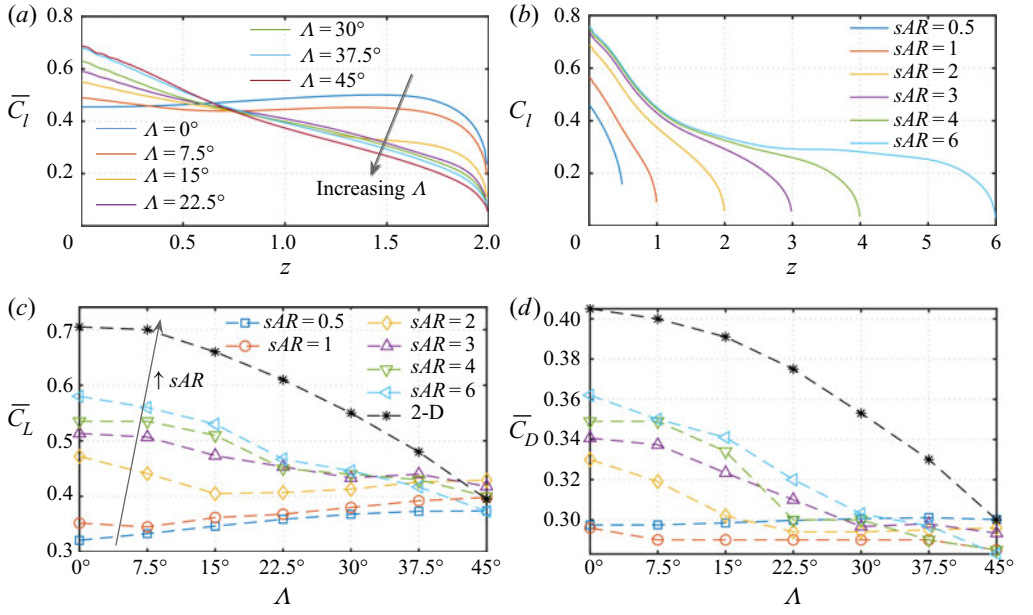


FIGURE 7. Force coefficients for $\alpha = 20°$. (*a*) Sectional lift coefficients for varied sweep angles at a fixed aspect ratio $sAR = 2$. (*b*) Sectional lift coefficients for cases of $\Lambda = 45°$ with different aspect ratios. (*c*,*d*) Lift coefficients $\overline{C_L}$ and drag coefficients $\overline{C_D}$, respectively, over sweep angle Λ for different aspect ratios.

The effects of aspect ratio on the distribution of sectional lift coefficients of swept wings are examined for the cases $(\alpha, \Lambda) = (20°, 45°)$ in figure 7(*b*). A monotonic decrease of sectional lift is observed across $sAR = 0.5$ to 6. The maximum sectional lift at midspan $z = 0$ increases with the aspect ratio, and eventually saturates as sAR reaches 3. This observation suggests that the tip effect is still noticeable for low-AR swept wings even though distinct tip vortices are not observed. For high-AR wings, the C_l–z curves feature steep slope over the inboard region, reflecting the weakening of the midspan effects. The slope becomes shallower towards the outboard, where midspan effects diminish. The streamwise finger-like structures described in § 3.3 do not have a noticeable influence on the lift, as indicated by the flatness of the C_l–z curves at the outboard span shown in figure 7(*b*).

Finally, we present the total lift $\overline{C_L}$ and drag $\overline{C_D}$ coefficients of the swept wings at $\alpha = 20°$ with different aspect ratios and varying sweep angles in figure 7(*c*,*d*). For swept wings with $sAR = 0.5$ and 1, the lift coefficients increase with sweep angle, due to the dominance of the midspan effects over the entire wing span. The drag coefficients of the low-aspect-ratio wings, on the other hand, do not show significant variations over the increase of sweep angle. It is interesting to note that $\overline{C_D}$ for $sAR = 0.5$ is higher than that for $sAR = 1$, an observation also reported in Taira & Colonius (2009). For wings with $sAR \gtrsim 3$, the contribution of the high sectional lift at the inboard region to the total lift force is overshadowed by the lower sectional lift at the outboard region. As a result, the lift coefficients of wings with high aspect ratio decrease with increasing sweep angle. A similar trend is also observed for the drag coefficients of high-aspect-ratio wings. While for wings with small Λ the lift coefficients $\overline{C_L}$ are positively related with sAR, at the highest sweep angle of $\Lambda = 45°$, the maximum lift coefficient is achieved with $sAR = 2$,

https://doi.org/10.1017/jfm.2020.778 Published online by Cambridge University Press

and is even higher than the analogous 2-D case. The midspan effects as lift enhancement mechanism for low-aspect-ratio swept wings could potentially inspire designs of high-lift devices.

4. Conclusion

We have studied laminar separated flows over finite-aspect-ratio swept wings with direct numerical simulations at a chord-based Reynolds number of 400. Owing to the complex interplay between the effects of aspect ratio, sweep angle and angle of attack, the wakes of finite swept wings exhibit a variety of vortical features, which are not observed behind unswept wings. We have described key mechanisms that are responsible for the emergence of different types of flows over swept wings. For wings with low aspect ratios and low sweep angles, the downwash by the tip vortices stabilizes the wake. With the increase in aspect ratio, the downwash weakens along the midspan, allowing the formation of unsteady vortex shedding. For higher sweep angles, the source of three-dimensionality in the wake transitions from the wing tip to the midspan. Three-dimensional flows featured by a pair of symmetric vortical structures form near the midspan due to the induced downward velocity. Such midspan effects not only stabilize the wake of higher-aspect-ratio swept wings, but also can act as a lift enhancement mechanism for wings with low to medium aspect ratios. At high aspect ratio, the midspan effects diminish near the outboard of the wing, and unsteady vortex shedding occurs near the wing tip region. For wings with high aspect ratios, steady wakes are again achieved at high sweep angles, where a transposition occurs from 2-D unsteady flow to three-dimensional steady flow. The resulting steady wake features the repetitive formation of the streamwise finger-like structures along the span.

This study provided a detailed look into the effects of sweep on the wake dynamics of finite-aspect-ratio wings. The insights obtained from this study, particularly those regarding the midspan effects, could potentially be used for designing high-lift devices. In addition, the knowledge gained here also forms a stepping stone for further understanding the complex wake dynamics at higher Reynolds numbers and those generated by unsteady wing manoeuvres.

Acknowledgements

We acknowledge the generous support from the US Air Force Office of Scientific Research (FA9550-17-1-0222) monitored by Dr G. Abate.

Declaration of interest

The authors report no conflict of interest.

References

Beem, H. R., Rival, D. E. & Triantafyllou, M. S. 2012 On the stabilization of leading-edge vortices with spanwise flow. *Exp. Fluids* **52** (2), 511–517.

Ben-Gida, H., Gurka, R. & Weihs, D. 2020 Leading-edge vortex as a high-lift mechanism for large-aspect-ratio wings. *AIAA J.* **58** (7), 2806–2819.

Black, J. 1956 Flow studies of the leading edge stall on a swept-back wing at high incidence. *Aeronaut. J.* **60** (541), 51–60.

https://doi.org/10.1017/jfm.2020.778 Published online by Cambridge University Press

DeVoria, A. C. & Mohseni, K. 2017 On the mechanism of high-incidence lift generation for steadily translating low-aspect-ratio wings. *J. Fluid Mech.* **813**, 110–126.

Eldredge, J. D. & Jones, A. R. 2019 Leading-edge vortices: mechanics and modeling. *Annu. Rev. Fluid Mech.* **51** (1), 75–104.

Garmann, D. J. & Visbal, M. R. 2020 Examination of pitch-plunge equivalence for dynamic stall over swept finite wings. *AIAA Paper* 2020-1759.

Gursul, I. 2005 Review of unsteady vortex flows over slender delta wings. *J. Aircraft* **42** (2), 299–319.

Gursul, I., Gordnier, R. & Visbal, M. 2005 Unsteady aerodynamics of nonslender delta wings. *Prog. Aerosp. Sci.* **41** (7), 515–557.

Ham, F. & Iaccarino, G. 2004 Energy conservation in collocated discretization schemes on unstructured meshes. In *Annual Research Briefs, Center for Turbulence Research*, pp. 3–14.

Ham, F., Mattsson, K. & Iaccarino, G. 2006 Accurate and stable finite volume operators for unstructured flow solvers. In *Annual Research Briefs, Center for Turbulence Research*, pp. 243–261.

Harper, C. W. & Maki, R. L. 1964 A review of the stall characteristics of swept wings. *NASA Tech. Note* D-2373.

Jardin, T. 2017 Coriolis effect and the attachment of the leading edge vortex. *J. Fluid Mech.* **820**, 312–340.

Lambert, W. B., Stanek, M. J., Gurka, R. & Hackett, E. E. 2019 Leading-edge vortices over swept-back wings with varying sweep geometries. *R. Soc. Open Sci.* **6** (7), 190514.

Lentink, D. & Dickinson, M. H. 2009 Rotational accelerations stabilize leading edge vortices on revolving fly wings. *J. Expl Biol.* **212** (16), 2705–2719.

Lentink, D., Müller, U. K., Stamhuis, E. J., De Kat, R., Van Gestel, W., Veldhuis, L. L. M., Henningsson, P., Hedenström, A., Videler, J. J. & Van Leeuwen, J. L. 2007 How swifts control their glide performance with morphing wings. *Nature* **446** (7139), 1082–1085.

Mulleners, K., Mancini, P. & Jones, A. R. 2017 Flow development on a flat-plate wing subjected to a streamwise acceleration. *AIAA J.* **55** (6), 2118–2122.

Nickel, K. & Wohlfahrt, M. 1994 *Tailless Aircraft in Theory and Practice*. AIAA.

Polhamus, E. C. 1966 A concept of the vortex lift of sharp-edge delta wings based on a leading-edge-suction analogy. *NASA Tech. Note* D-3736.

Rockwell, D. 1993 Three-dimensional flow structure on delta wings at high angle-of-attack: experimental concepts and issues. *AIAA Paper* 1993-0550.

Sarpkaya, T. 1966 Separated flow about lifting bodies and impulsive flow about cylinders. *AIAA J.* **4** (3), 414–420.

Schlichting, H. & Truckenbrodt, E. 1960 *Aerodynamik des Flugzeuges: Grundlagen aus der Strömungsmechanik, Aerodynamik des Tragflügels (Teil II)*. Springer.

Taira, K. & Colonius, T. 2009 Three-dimensional flows around low-aspect-ratio flat-plate wings at low Reynolds numbers. *J. Fluid Mech.* **623**, 187–207.

Thomson, K. D. & Morrison, D. F. 1971 The spacing, position and strength of vortices in the wake of slender cylindrical bodies at large incidence. *J. Fluid Mech.* **50** (4), 751–783.

Videler, J. J., Stamhuis, E. J. & Povel, G. D. E. 2004 Leading-edge vortex lifts swifts. *Science* **306** (5703), 1960–1962.

Visbal, M. R. & Garmann, D. J. 2019 Effect of sweep on dynamic stall of a pitching finite-aspect-ratio wing. *AIAA J.* **57** (8), 3274–3289.

Winkelmann, A., Barlow, J., Saini, J., Anderson, J. Jr. & Jones, E. 1980 The effects of leading edge modifications on the post-stall characteristics of wings. *AIAA Paper* 1980-0199.

Yen, S. C. & Hsu, C. M. 2007 Flow patterns and wake structure of a swept-back wing. *AIAA J.* **45** (1), 228–236.

Yen, S. C. & Huang, L. C. 2009 Flow patterns and aerodynamic performance of unswept and swept-back wings. *J. Fluids Engng* **131** (11), 111101.

Zhang, K., Hayostek, S., Amitay, M., He, W., Theofilis, V. & Taira, K. 2020 On the formation of three-dimensional separated flows over wings under tip effects. *J. Fluid Mech.* **895**, A9.

Zhang, S., Jaworski, A. J., McParlin, S. C. & Turner, J. T. 2019 Experimental investigation of the flow structures over a 40° swept wing. *Aeronaut. J.* **123** (1259), 39–55.

https://doi.org/10.1017/jfm.2020.778 Published online by Cambridge University Press